Journal of
Materials Chemistry A

PAPER

View Article Online
View Journal | View Issue

Cite this: *J. Mater. Chem. A*, 2019, 7, 16728

Semiconductor TiO_2 thin film as an electrolyte for fuel cells†

Wenjing Dong,[a] Yuzhu Tong,[a] Bin Zhu,*[abc] Haibo Xiao,[a] Lili Wei,[a]
Chao Huang,[a] Baoyuan Wang,[a] Xunying Wang,[a] Jung-Sik Kim[c]
and Hao Wang*[a]

Received 20th February 2019
Accepted 11th June 2019

DOI: 10.1039/c9ta01941c

rsc.li/materials-a

Electrolyte layer, made up of an ionic conductor with ignorable electronic conductivity, plays vital roles in transporting ions as well as blocking electron passage in electrochemical devices like a solid oxide fuel cell (SOFC). The electronic conductivity of the electrolyte has been always blamed for bringing in the short-circuiting problem. In this study, however, we demonstrate that the dominant issue is not the electronic conductivity of electrolytes but the energy band diagram of the device. Using a semiconductor TiO_2 thin film as an electrolyte, we present a novel design of fuel cell devices from the perspective of the energy band structure and alignment. A TiO_2 thin film was fabricated by a mass-productive spin coating method. An OCV of 1.1 V and maximum power output of 364 mW cm^{-2} at 550 °C were achieved, which proves that TiO_2 plays the role of an electrolyte with sufficient ionic transportation while no electronic short-circuiting problem occurs. The online intercalation of Li into TiO_2 enables the creation of more oxygen vacancies. Additionally, proton incorporation and conducting mechanisms in TiO_2 have been verified and discussed. This work provides a new method for suppressing the electronic conductivity of electrolytes as well as developing functional electrolytes from a well-known semiconductor for advanced low-temperature SOFCs.

1. Introduction

Lowering the operating temperature of a solid oxide fuel cell (SOFC) is an inevitable trend towards its commercialization through worldwide research, which results in the necessity of developing low temperature oxygen ion or proton conductive materials. The steady progress of the ionic conductor is enormously contributed by doping technology. By properly selecting the doping elements, doping can significantly enhance the stability of materials. It is well known that doping Y into ZrO_2 stabilizes the structure of ZrO_2 (YSZ),[1] and doping Er into Bi_2O_3 helps to stabilize the δ-phase.[2,3] Another purpose of doping is to improve the ionic conductivity by increasing the oxygen vacancy concentration in the material. Doped CeO_2 and Sr- and Mg-doped $LaGaO_3$ (LSGM) are reported to possess high ionic conductivity at low temperatures.[4] However, they are often limited by their instability and incapability of suppressing electronic leakage when exposed to the reduced atmosphere.

Traditionally, the electronic conductivity of the electrolyte is considered catastrophic because the short-circuiting problem in SOFC is thought to be originated from it.[5,6] However, interestingly, for some researchers, the electronic conductivity of electrolytes doesn't seem to be an obstacle in their creative design. Zhu *et al.* found that no short-circuiting occurred in the cells that use semiconductor-ionic conductor composites as electrolytes.[7–9] Besides, some highly electronic conductive materials have been reported to function as electrolytes to realize fuel cell reactions. Zhou *et al.* reported that a strongly correlated perovskite fuel cell using $SmNiO_3$ with high initial electronic conductivity as electrolyte layer obtained 225 mW cm^{-2} at 500 °C in a single layer configuration Pt/$SmNiO_3$/Pt.[10] Tao *et al.* also achieved electrolyte function from an electronic conductor.[11,12] These experimental data suggest that using electronic conductors as an electrolyte is obviously acceptable, but how to suppress their electronic leakage in a fuel cell environment is a critical issue.

Since short-circuiting problems in SOFC results from the electron transportation in an electrolyte, manipulating electron transportation behavior should be the top priority in designing SOFC. Theoretically, electron transportation in a single material is dominated by the conductivity of the material. However, in a device fabricated from different kinds of materials, the conductivity of the materials will no longer be the only

---

[a] *Key Laboratory of Ferro, Piezoelectric Materials and Devices of Hubei Province, Faculty of Physics and Electronic Science, Hubei University, Wuhan, Hubei 430062, P. R. China. E-mail: zhubin@hubu.edu.cn; binzhu@kth.se; wangh@hubu.edu.cn*

[b] *Faculty of Materials Science and Chemistry, China University of Geosciences, 388 Lumo Road, Wuhan 430074, China*

[c] *Department of Aero & Auto Engineering, Loughborough University, Ashby Road, Loughborough, LE11 3TU, UK*

† Electronic supplementary information (ESI) available. See DOI: 10.1039/c9ta01941c

dominator in electron transportation. Taking a typical semiconductor p–n junction as an example, though the p- and n-type semiconductors have non-negligible electronic conductivity, the p–n junction is cut off in the reverse condition, namely, the reverse resistance is enormously larger compared with the forward resistance. So, in SOFC, a three-layer device, we cannot simply blame its short-circuiting problem on the electronic conductivity of the electrolyte. As the transportation behavior of electrons is closely related to the energy band structures of materials in the device from the perspective of solid state physics, short-circuiting problem might be solved from energy band engineering, which has already been utilized in various fields to manipulate charge carrier transportation. In a semiconductor device like solar cells, the energy band diagram is carefully designed to facilitate the transportation of electrons and holes.[13,14] In electrochemical devices for applications such as photoelectrochemical (PEC) water splitting, the energy levels of the photoanode and counter electrode are also required to obey the critical rules.[15] Apart from electronic devices, the role of energy band diagram has also gradually drawn researchers' awareness in ionic devices. For example, in Li batteries, the electrochemical potential of the anode and cathode should match with the energy level of the electrolyte in order to avoid electrolyte reduction on the anode or oxidization on the cathode.[16]

In this study, we applied a semiconductor thin film as the electrolyte layer of SOFC. Since the electron transportation in a semiconductor is highly affected by the energy band structure, we can suppress the electronic conduction by properly selecting the band structure of the anode and cathode material. In order to lower the operating temperature of SOFC, effectively reducing the thickness of the electrolyte is an efficient way.[17,18] Among all thin film technologies, mass-productivity should be taken into consideration in seek of commercialization. Fabricated by a spin-coating method, a typical semiconductor TiO_2 thin film is used as an electrolyte. We designed the band structure of SOFC in comparison with that of a PEC water splitting device in order to avoid electron short-circuiting problems. Spontaneous ion doping in TiO_2 is also demonstrated to be helpful in increasing its ionic conductivity. The fuel cell can deliver good current and power outputs, which are valuable for various studies. We believe that this study will be beneficial in extending semiconductors' applications in advanced SOFCs and solid state ionic devices.

2. Experimental

2.1 Material preparation and fuel cell fabrication

Firstly, commercial $LiNi_{0.8}Co_{0.15}Al_{0.05}O_2$ (NCAL) powders added by 3 wt% polyvinylidene fluoride (PVDF) as a binder were pressed into a ϕ 13 mm pellet with a thickness of 0.57 mm under the pressure of 200–300 MPa. NCAL was purchased from Tianjing-Bamo Company, and PVDF from Sinopharm Chemical Reagent Co., Ltd. After annealing at 500 °C for 2 h to remove PVDF, the pellet was then used as the device anode substrate. TiO_2 film was fabricated on the substrate by the decomposition of titanium diisopropoxidebis(acetylacetonate) according to our previous report.[13] It is a widely applied method in solar cells. Specifically, a solution of titanium diisopropoxidebis(acetylacetonate) (in 75% isopropanol, HeptaChroma) (TDB) diluted in ethanol (1 : 3, volume ratio) was spin-coated on the anode pellet with a speed of 1500 rads^{-1} for 30 s. The spin coating process was repeated 10–20 times. Then, the sample was annealed at 500 °C for 30 min to form a TiO_2 thin film electrolyte layer. This sample is named as "TiO_2 on NCAL" (TON) in the following text. The cathode layer was made with Ni foam coated with NCAL (Ni-NCAL). To be specific, NCAL powder was uniformly dispersed in terpineol to form a slurry, which was then brush-coated on Ni-foam, followed by desiccation at 120 °C. The Ni-NCAL cathode was then pressed into a thin pellet, and assembled with the above TON sample to form a fuel cell device with a configuration of NCAL/ TiO_2/ Ni-NCAL. The effective area of the fuel cell device was 0.64 cm^2.

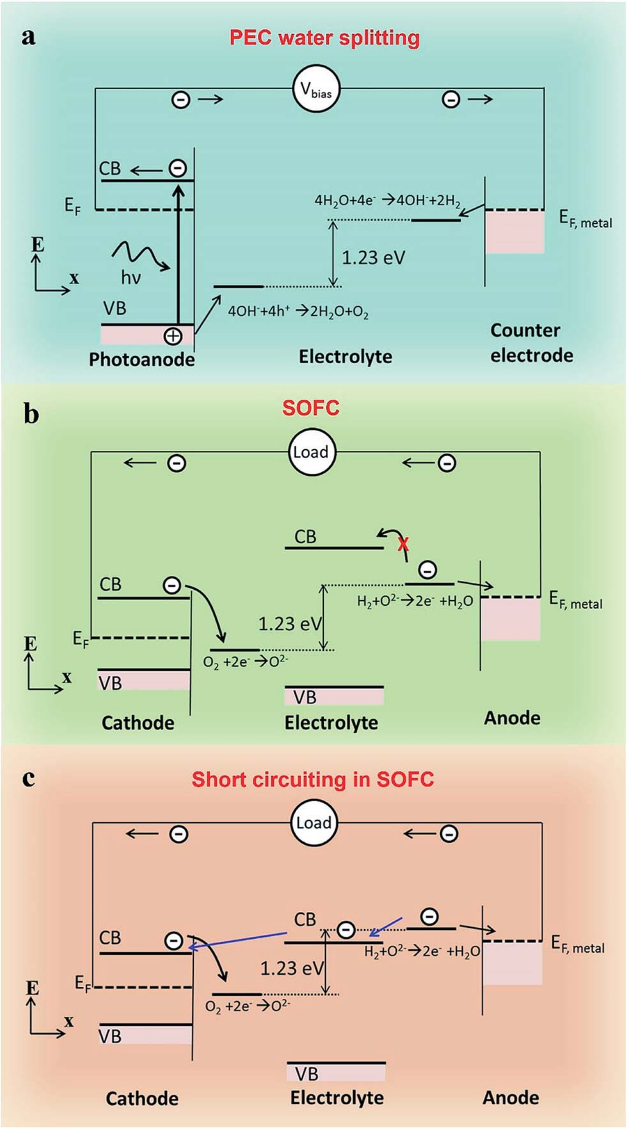

Fig. 1 Energy band diagrams of (a) PEC water splitting (Honda–Fujishima effect), (b) SOFC, and (c) SOFC with the occurrence of short circuiting. If the anode of SOFC is not a metal but a semiconductor instead, the CB level of this semiconductor should be lower than the energy level of H^+/H_2 as the electrons generated by H_2 oxidation are expected to flow to the CB level of this semiconductor.

2.2 Material characterization

The crystal structures of the as-prepared solid samples were detected by X-ray diffraction (XRD) using Bruker D8 advanced X-ray diffractometer (Germany, Bruker Corporation) with Cu Ka radiation ($\lambda = 1.54060$ Å) as the source. The morphologies and microstructures of the samples were analyzed by JSM7100F field emission scanning electron microscope (FESEM) and FEI Tecnai G2 F30 transmission electron microscope (TEM). X-ray photoelectron spectroscopy (XPS) and ultraviolet photoelectron spectroscopy (UPS) were carried out on an ESCALAB 250Xi photoelectron spectrometer (Thermo Fisher Scientific, UK). The optical energy bandgap of the materials was estimated by UV-vis-NIR absorption test carried out on UV3600. NCAL was pressed into a pellet for XPS and UPS tests and a TiO_2 thin film was fabricated on an NCAL substrate as well as on Si and glass substrates for relative tests.

2.3 Electrical and electrochemical tests of fuel cell

The cell performance, characterized by *I–V* (current density–voltage) and *I–P* (current density–power density) curves, was measured by the programmable electronic load using a computerized instrument (IT8511, ITECH) at 550 °C. During the test, pure hydrogen and air were used as fuel and oxidant gas, respectively. The gas flow rates were kept in the range of 120–150 mL min^{-1} for H_2 and ~150 mL min^{-1} for air. The electrochemical impedance spectra (EIS) measurements were tested in the same gas atmosphere as above using an electrochemical work station (Gamry Reference 3000, USA) under OCV mode. The measured frequency range was 1 MHz–0.1 Hz, while the amplitude was 10 mV.

3. Results and discussion

3.1 Fuel cell design from energy band structure

According to the energy band theory, in order to adjust the carrier transportation behavior in a device, materials with different energy band structures should be carefully designed. For example, in a PEC water splitting device, the Fermi level of the metal counter electrode must be higher than the redox potential of H^+/H_2 while the valence band (VB) level of a semiconductor photoanode is required to be lower than the redox potential of H_2O/O_2 (Fig. 1a).[15] As we know, the fuel cell reaction can be regarded as a reverse reaction of water splitting. In a typical SOFC, electrons are generated at the anode/electrolyte interface and are then supposed to flow through the anode to the outer circuit when the circuit is connected. In the meantime, no electrons are expected to flow through the electrolyte, otherwise, short-circuiting occurs (Fig. 1b). So the electrons in the anode should be blocked by the electrolyte from the perspective of energy band theory. In a typical Ni-YSZ (Y-stabilized ZrO_2) fuel cell, the redox potential of H_2/H^+ is about −4.5 eV relative to vacuum energy (RVE), and the work function for a typical anode material Ni is about −5.1 eV RVE, which is lower than the potential of H_2/H^+, and hence electrons stemmed from the oxidation of H_2 can flow to the anode. In the meantime, the conduction band (CB) of YSZ electrolyte is higher than the redox potential of H_2/H^+;[19,20] electrons cannot jump to the CB of the electrolyte, namely the electrons that are blocked by the electrolyte. However, if an electrolyte material has lower CB level, short-circuiting problem might occur (Fig. 1c). For example, the CB level of SDC, which is measured to be at around −5.65 eV (Fig. S1†), is much lower than −4.5 eV, and the short-

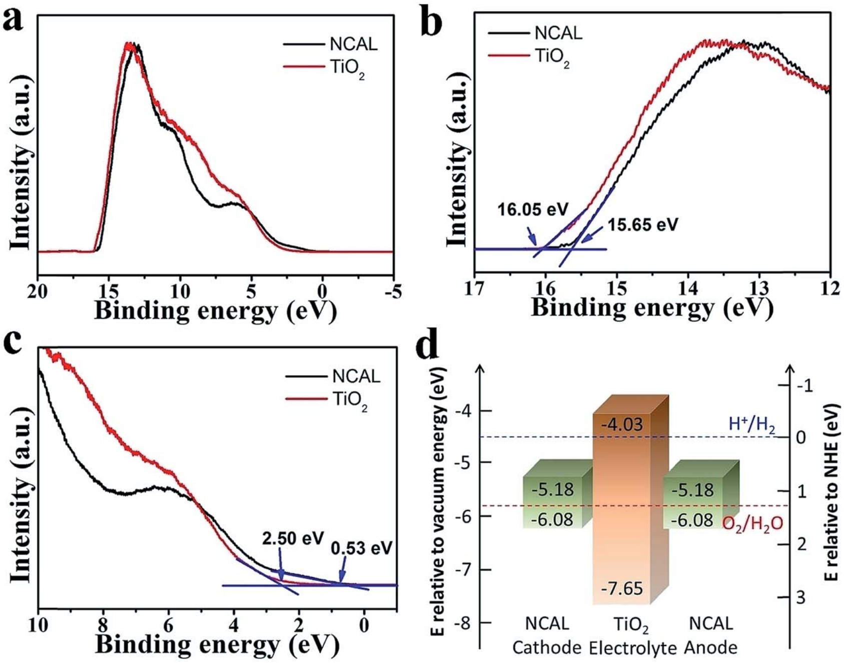

Fig. 2 UPS spectra of NCAL and TiO_2: (a) complete spectrum, (b) cutoff energy region, and (c) onset energy region. (d) Energy band diagram of fuel cell NCAL/TiO_2/NCAL obtained according to UPS results and energy band gap.

circuiting problem was often observed in the SDC electrolyte fuel cell. However, as the electronic conductivity of SDC is rather low, short-circuiting doesn't occur at first. But when SDC is reduced by H_2, its electronic conductivity would rapidly increase and electrons can flow through it.[21] That is why short-circuiting problem was observed in an SDC electrolyte fuel cell after a period of operation. In short, the energy band structure of a good SOFC should obey the following rules: (1) the CB level of the electrolyte should be higher than the redox potential of H_2/H^+, (2) the Fermi level of the metal anode (or the CB level of semiconductor anode) should be lower than the redox potential of H_2/H^+, (3) the valence band (VB) level of the electrolyte should be lower than the redox potential of O_2/O^{2-}, (4) the CB level of the cathode should be higher than the redox potential of O_2/O^{2-}.

3.2 Fuel cell fabrication and characterization

According to the above rules, using a typical n-type semiconductor TiO_2, whose CB level is higher than −4.5 eV RVE, as the electrolyte, we carefully considered the energy band structure of the electrode materials. Finally, a triple (oxygen ionic, protonic, and electronic) conductive semiconductor NCAL[22] was applied as both the anode and cathode. From UPS and UV-vis-NIR results, the energy band diagram of a thin film TiO_2 electrolyte fuel cell with NCAL electrodes was elucidated in Fig. 2d. According to $\varphi = 21.2\text{ eV} - (E_{\text{cutoff}} - E_{\text{onset}})$,[23] where E_{cutoff} is the cutoff energy and E_{onset} is the onset energy from UPS (Fig. 2b and c), the VB levels of NCAL and TiO_2 are calculated to be −6.08 and −7.65 eV RVE, respectively. The CB levels are obtained as −5.18 eV for NCAL and −4.03 eV for TiO_2, by subtracting E_g from VB levels, where E_g is the optical energy gap obtained from optical absorbance spectra (Fig. S2†). From the energy band diagram presented in Fig. 2d, the energy levels of the three parts match well with all rules stated above.

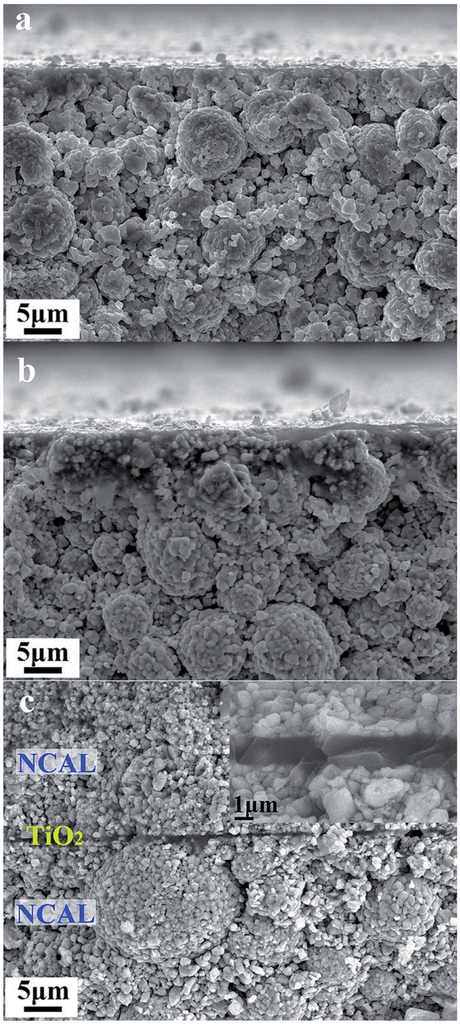

Fig. 3 Cross sectional view; SEM images of (a) pure NCAL pellet, (b) TiO_2 thin film fabricated on NCAL pellet, and (c) TiO_2 electrolyte fuel cell.

Fig. 3 shows the SEM morphologies of pure NCAL substrate and TiO_2 thin film fabricated on NCAL. NCAL powders are spherical particles and the dry-pressed pellet was not very compact with some voids existing between the particles. Such porous structure is actually desired for the fuel cell anode to enhance the catalyst function. When spin coating TiO_2 solution on the pellet, it partially infiltrated into the pores of the NCAL substrate. From Fig. 3b, we can see that a thin film was formed within a certain depth of the NCAL substrate. Raman tests further verified that the thin film on NCAL was TiO_2 (Fig. S3†). The cross section of the TiO_2 electrolyte fuel cell is presented in Fig. 3c. It can be observed that a compact TiO_2 thin film was sandwiched between two NCAL layers, separating the anode and cathode.

The typical *I–V–P* characteristics of the TiO_2 thin film electrolyte fuel cell measured at 550 °C are shown in Fig. 4a. An OCV

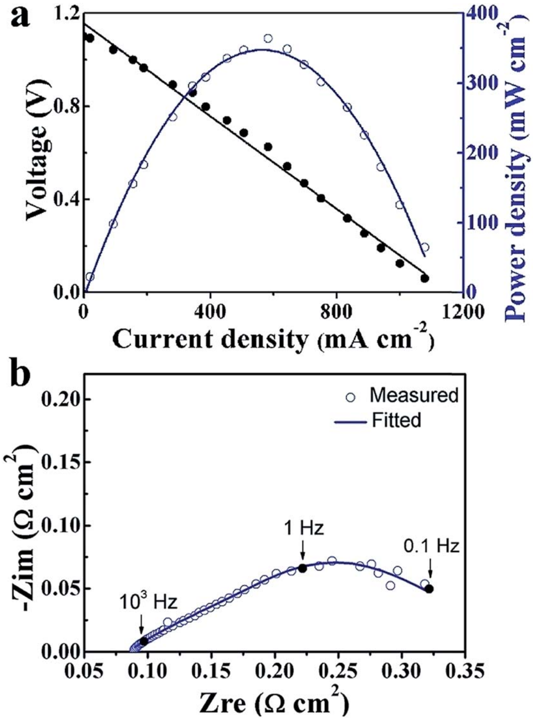

Fig. 4 (a) *I–V* and *I–P* characteristics and (b) EIS spectra of the TiO_2 thin film electrolyte fuel cell measured at 550 °C.

of 1.1 V and a maximum power density (P_{max}) of 364 mW cm^{-2} were obtained. The OCV value provides clear evidence that the designed energy band alignment succeeded in solving the electronic short-circuiting problem in the device. By contrast, the fuel cell made without the TiO_2 thin film, *i.e.* the assembly of the NCAL substrates and Ni-NCAL cathode in the configuration of NCAL/Ni-NCAL, showed no OCV or detectable power output. This provides further support for TiO_2 acting as the electrolyte to conduct ions, resulting in OCVs and power outputs. EIS result is presented in Fig. 4b. The fitting curve is in good agreement with the measured EIS, where R_0, relating to the intercept of the impedance arc on the real axis, represents the bulk resistance (or ohmic resistance) of the cell. From the capacitance calculated from R and Q, the high frequency and low frequency resistance, R_1 and R_2, can be assigned to the mass transfer resistance, including gas diffusion.[24,25] No significant grain boundary resistance arc was observed for the TiO_2 electrolyte device, suggesting good ionic conductivity of TiO_2. A more detailed discussion on the EIS for the TiO_2 electrolyte cell taken under different voltage conditions is presented in Fig. S4.†

3.3 Ionic conductive property analysis of TiO_2

In a typical proton conductive perovskite oxide, protons can bond with oxygen to form ionic defects ($OH_O^{\bullet}$in Kröger–Vink notation).

$$H_2O + V_O^{\bullet\bullet} + O_O^{\times} \rightarrow 2OH_O^{\bullet} \tag{1}$$

Then, protons diffuse in the material through the processes involving rotational diffusion of the proton defects and transfer to the neighboring oxygen ions, which is frequently termed as Grotthuss mechanism.[26] In TiO_2, proton incorporation and diffusion along the *c*-axis of TiO_2 happen in a similar way, albeit with some differences in the proton incorporation process. The processes have been schematized in Fig. 5: (i) proton incorporation: theoretical calculation shows that the existence of oxygen vacancies allows electrons to move from the vacancies to the neighboring Ti and O sites in TiO_2;[27] thus, the electron density around the O neighboring to oxygen vacancies is high, so protons will prefer to incorporate into TiO_2 by forming an OH bond with O at the shared edge of Ti^{3+} and Ti^{4+} (overall reaction $H^+ + V_O^{\bullet\bullet} + O_O^{\times} \rightarrow OH_O^{\bullet} + V_O^{\bullet\bullet}$);[28] (ii) rotational diffusion; (iii) transfer to neighboring oxygen, (iv) bending and (v) elongation of the Ti–O bond. According to the above processes, the proton conductivity of TiO_2 is closely related to the oxygen vacancies in it.

In our case, slight Li_2CO_3 fragments were observed on the surfaces of NCAL, which is consistent with previous reports (Fig. 6a).[29] Thus Li will possibly incorporate into TiO_2 during its fabrication process (Fig. 6b).[30] Li-insertion in TiO_2 has already been broadly reported.[31,32] As the valence state of Li^+ is much lower than that of Ti^{4+}, more oxygen vacancies would be generated when Li^+ is intercalated into TiO_2 according to the following reaction.

$$2Ti^{4+} + Li^+ \rightarrow 2Ti^{3+} + Li_i^{\bullet} + V_o^{\bullet\bullet} \tag{2}$$

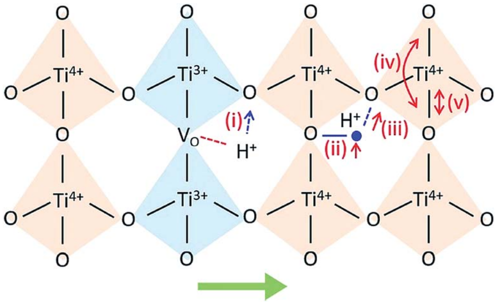

Fig. 5 Proton incorporation and conduction mechanisms in TiO_2. (i) Proton incorporation, (ii) rotational diffusion; (iii) transfer to neighboring oxygen, (iv) bending and (v) elongation of the Ti–O bond. The green arrow in the bottom points to the c-channel axis.

The existence of more oxygen vacancies in TiO_2 that is fabricated on NCAL than normal TiO_2 (TiO_2 on Si) was also proved by XPS results.

Fig. 7a shows Ti 2p XPS spectra of TiO_2 on Si (TOS) and TiO_2 on NCAL (TON). Due to the electronic spin–orbit coupling, the Ti 2p orbitals split into two energy levels, 2p1/2 (noted as 2p1) and 2p3/2 (noted as 2p3).[33] The peaks located at 458.4 and 464.4 eV are assigned to Ti^{4+} 2p3 and Ti^{4+} 2p1, respectively. The peaks at 457.9 and 463.7 eV are attributed to the reduced state (Ti^{3+}).[34,35] The sum of Ti^{3+} peak area ratio of TON is much higher than that of TOS, demonstrating that the TiO_2 film formed on NCAL substrate has much lower valence state comparing with TiO_2 formed on Si substrate.[36] Fig. 7b shows the O 1s core level spectra of NCAL, TOS, and TON. It can be clearly observed that the O 1s peak of TON is much different from that of the NCAL

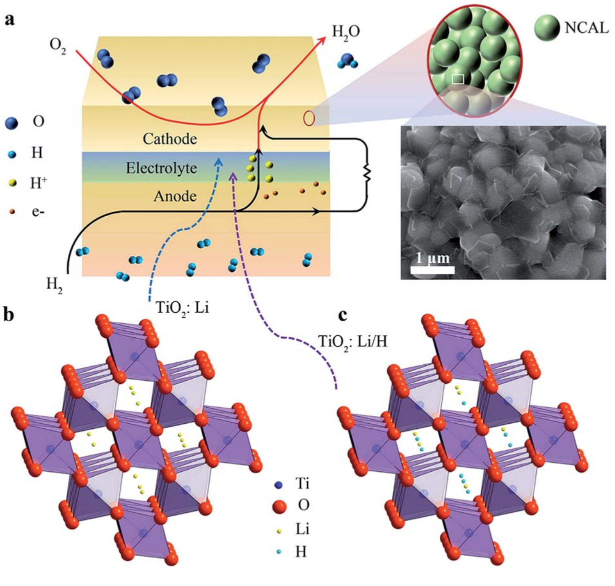

Fig. 6 (a) Schematic diagrams (not to scale) of the structure of TiO_2 thin film electrolyte fuel cell, the enlarged ones are the schematic structure of NCAL and the SEM image of the surface of NCAL particle. (b) The structure of TiO_2 crystal with the intercalation of Li that occupy the channels, and (c) the structure of TiO_2 crystal with the intercalation of both Li and H that occupy the channels.

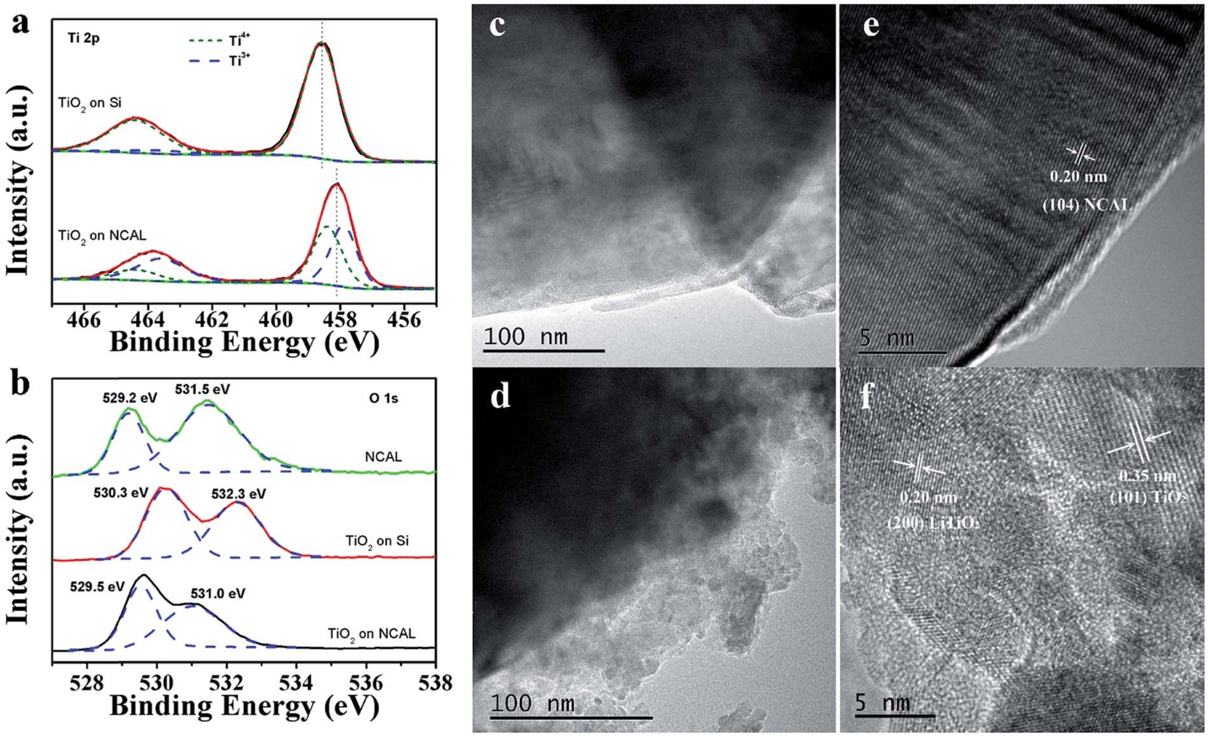

Fig. 7 (a) Ti 2p XPS spectra of TiO_2 on Si and TiO_2 on NCAL annealed at 550 °C for 30 min. (b) O 1s core level XPS spectra of NCAL, TiO_2 on Si, and TiO_2 on NCAL. TEM images of (c and e) NCAL and (d and f) core shell structure of TiO_2 fabricated on NCAL particles.

and TiO_2 on Si, indicating its different bonding environments of O species. Compared with TOS, the binding energy (BE) of O 1s of TON was negatively shifted. The Ti–O–Ti is observed at 529.5 eV for TON and this reduced value compared to TOS is attributed to the existence of enormous amount of oxygen vacancies.[37,38] The higher BE peaks are associated with the –OH species.[39,40]According to previous reports, the ionic conductivity of oxides is closely related to the O 1s BE.[41–43] Barr[42] divided oxides into three different types based on their O 1s BE, and oxides with BE in the range of 528.0–529.5 eV were regarded as very ionic oxides. From Fig. 7b, it can be observed that the low energy O 1s peak of TON and NCAL are all lower than 529.5 eV, indicating that both of them can be assigned to the "very ionic oxide" type. Comparing with NCAL whose ionic conductivity has already been proven,[44] the area ratio of the low energy peak to the high energy peak of TON is much larger, suggesting that the TiO_2 film also has good ionic conductivity.

Li doping in TiO_2 has also been proved from TEM test. For pure NCAL particles, only the (104) face (d = 0.20 nm) was detected. However, for TiO_2 coating on NCAL particle, besides the observation of the (101) face of anatase TiO_2, a lattice distance of 0.20 nm, which denotes the (200) face of $LiTiO_2$,[30] was also found. In the fuel cell environment, protons generated by the anode reaction might possibly exchange with Li^+ in TiO_2: Li, forming TiO_2: Li/H (Fig. 6c) as reported in other lithium titanate. It is reported for $Li_2Ti_3O_7$ that when Li^+ is replaced by H^+, $H_2Ti_3O_7$ will form, which has been proved to be a proton conductor.[45] Besides, during the fuel cell reaction process at 550 °C studied by us, TiO_2 might be in a rutile phase as the temperature of anatase to rutile transformation is between 500–600 °C.[46] The intercalation of hydrogen in the c channels of rutile TiO_2 and its motion in TiO_2 have also been reported.[28,47] Reports have revealed that the activation energy for H migration along the c-channel of rutile TiO_2 is 0.5–0.6 eV for diffusion,[47,48] which is comparative to the activation energy of proton conduction in $BaCe_{0.8-x}Zr_xY_{0.2}O_{3-\delta}$.[49] In addition, using typical proton conductor, BZCY (($BaZr_{0.1}Ce_{0.7}Y_{0.2}O_3$)), as H^+ filtering layer to allow only protons to pass, the proton conduction in TiO_2 electrolyte has been verified (Fig. S5 and 6†).

4. Conclusions

TiO_2 thin film has been successfully fabricated by a mass-productive spin coating method for novel fuel cell device applications. The TiO_2 electrolyte fuel cell was designed using the energy band theory and has a typical combination of semiconductor and ion properties with fuel cells. The TiO_2 thin film fuel cell has manifested a notable yield of 364 mW cm^{-2} at 550 °C. With more oxygen vacancies created, the online intercalation of Li into TiO_2 promoted its proton conductivity. This work provides a new idea for constructing LT-SOFC and will hopefully provoke more investigations on exploring the ionic conductivity of semiconductor materials to make new technological breakthroughs for their applications.

Conflicts of interest

There are no conflicts to declare.

Acknowledgements

This work was supported by the National Natural Science Foundation of China (NSFC, No. 11604088 and 51772080). The authors thank Hubei Provincial 100-Talent Distinguished Professor Grant.

References

1 S. P. S. Badwal, *Solid State Ionics*, 1992, **52**, 23–32.

2 K. Shitara, T. Moriasa, A. Sumitani, A. Seko, H. Hayashi, Y. Koyama, R. Huang, D. Han, H. Moriwake and I. Tanaka, *Chem. Mater.*, 2017, **29**, 3763–3768.

3 S. Sanna, V. Esposito, J. W. Andreasen, J. Hjelm, W. Zhang, T. Kasama, S. B. Simonsen, M. Christensen, S. Linderoth and N. Pryds, *Nat. Mater.*, 2015, **14**, 500.

4 Z. Gao, L. V. Mogni, E. C. Miller, J. G. Railsback and S. A. Barnett, *Energy Environ. Sci.*, 2016, **9**, 1602–1644.

5 M. Gödickemeier and L. J. Gauckler, *J. Electrochem. Soc.*, 1998, **145**, 414–421.

6 M. H. D. Othman, N. Droushiotis, Z. Wu, G. Kelsall and K. Li, *Adv. Mater.*, 2011, **23**, 2480–2483.

7 B. Zhu, R. Raza, H. Qin, Q. Liu and L. Fan, *Energy Environ. Sci.*, 2011, **4**, 2986–2992.

8 B. Zhu, P. D. Lund, R. Raza, Y. Ma, L. Fan, M. Afzal, J. Patakangas, Y. He, Y. Zhao, W. Tan, Q.-A. Huang, J. Zhang and H. Wang, *Adv. Energy Mater.*, 2015, **5**, 1401895.

9 B. Zhu, Y. Huang, L. Fan, Y. Ma, B. Wang, C. Xia, M. Afzal, B. Zhang, W. Dong, H. Wang and P. D. Lund, *Nano Energy*, 2016, **19**, 156–164.

10 Y. Zhou, X. Guan, H. Zhou, K. Ramadoss, S. Adam, H. Liu, S. Lee, J. Shi, M. Tsuchiya, D. D. Fong and S. Ramanathan, *Nature*, 2016, **534**, 231–234.

11 R. Lan and S. Tao, *Adv. Energy Mater.*, 2014, **4**, 1301683.

12 R. Lan and S. Tao, *Chem.–Eur. J.*, 2015, **21**, 1350–1358.

13 W. Dong, T. Zhang, X. Chen, B. Wang and B. Zhu, *Phys. Status Solidi A*, 2017, **214**, 1700089.

14 H. Zhou, Q. Chen, G. Li, S. Luo, T.-b. Song, H.-S. Duan, Z. Hong, J. You, Y. Liu and Y. Yang, *Science*, 2014, **345**, 542–546.

15 A. Kudo and Y. Miseki, *Chem. Soc. Rev.*, 2009, **38**, 253–278.

16 C. Liu, Z. G. Neale and G. Cao, *Mater. Today Mater. Today*, 2016, **19**, 109–123.

17 E. D. Wachsman and K. T. Lee, *Science*, 2011, **334**, 935–939.

18 P.-C. Su, C.-C. Chao, J. H. Shim, R. Fasching and F. B. Prinz, *Nano Lett.*, 2008, **8**, 2289–2292.

19 G. Liu, J. A. Rodriguez, J. Hrbek, J. Dvorak and C. H. F. Peden, *J. Phys. Chem. B*, 2001, **105**, 7762–7770.

20 P. D. C. King, T. D. Veal, S. A. Hatfield, P. H. Jefferson, C. F. McConville, C. E. Kendrick, C. H. Swartz and S. M. Durbin, *Appl. Phys. Lett.*, 2007, **91**, 112103.

21 X. Zhang, M. Robertson, C. Deĉes-Petit, W. Qu, O. Kesler, R. Maric and D. Ghosh, *J. Power Sources*, 2007, **164**, 668–677.

22 L. Fan and P.-C. Su, *J. Power Sources*, 2016, **306**, 369–377.

23 Z. a. Li, Z. Zhu, C.-C. Chueh, S. B. Jo, J. Luo, S.-H. Jang and A. K. Y. Jen, *J. Am. Chem. Soc.*, 2016, **138**, 11833–11839.

24 L. Fan, H. Zhang, M. Chen, C. Wang, H. Wang, M. Singh and B. Zhu, *Int. J. Hydrogen Energy*, 2013, **38**, 11398–11405.

25 H. Hu, Q. Lin, Z. Zhu, X. Liu, M. Afzal, Y. He and B. Zhu, *J. Power Sources*, 2015, **275**, 476–482.

26 K.-D. Kreuer, *Chem. Mater.*, 1996, **8**, 610–641.

27 L.-B. Mo, Y. Wang, Y. Bai, Q.-Y. Xiang, Q. Li, W.-Q. Yao, J.-O. Wang, K. Ibrahim, H.-H. Wang, C.-H. Wan and J.-L. Cao, *Sci. Rep.*, 2015, **5**, 17634.

28 M. V. Koudriachova, S. W. de Leeuw and N. M. Harrison, *Phys. Rev. B: Condens. Matter Mater. Phys.*, 2004, **70**, 165421.

29 K. Matsumoto, R. Kuzuo, K. Takeya and A. Yamanaka, *J. Power Sources*, 1999, **81–82**, 558–561.

30 Z. Wang, S. Huang, B. Chen, H. Wu and Y. Zhang, *J. Mat. Chem. A*, 2014, **2**, 19983–19987.

31 L. J. Hardwick, M. Holzapfel, P. Novák, L. Dupont and E. Baudrin, *Electrochim. Acta*, 2007, **52**, 5357–5367.

32 C. Arrouvel, S. C. Parker and M. S. Islam, *Chem. Mater.*, 2009, **21**, 4778–4783.

33 C. Zhang, H. Yu, Y. Li, Y. Gao, Y. Zhao, W. Song, Z. Shao and B. Yi, *ChemSusChem*, 2013, **6**, 659–666.

34 W.-D. Zhu, C.-W. Wang, J.-B. Chen, Y. Li and J. Wang, *Appl. Surf. Sci.*, 2014, **301**, 525–529.

35 X. Zhang, H. Tian, X. Wang, G. Xue, Z. Tian, J. Zhang, S. Yuan, T. Yu and Z. Zou, *Mater. Lett.*, 2013, **100**, 51–53.

36 N.-L. Wu, M.-S. Lee, Z.-J. Pon and J.-Z. Hsu, *J. Photochem. Photobiol., A*, 2004, **163**, 277–280.

37 S. G. Ullattil and P. Periyat, *J. Mat. Chem. A*, 2016, **4**, 5854–5858.

38 R. Ren, Z. Wen, S. Cui, Y. Hou, X. Guo and J. Chen, *Sci. Rep.*, 2015, **5**, 10714.

39 G. Wang, H. Wang, Y. Ling, Y. Tang, X. Yang, R. C. Fitzmorris, C. Wang, J. Z. Zhang and Y. Li, *Nano Lett.*, 2011, **11**, 3026–3033.

40 B. Bharti, S. Kumar, H.-N. Lee and R. Kumar, *Sci. Rep.*, 2016, **6**, 32355.

41 V. Dimitrov and T. Komatsu, *J. Solid State Chem.*, 2002, **163**, 100–112.

42 T. L. Barr, *Modern ESCA, The Principles and Practice of X-Ray Photoelectron Spectroscopy*, CRS Press, Boca Raton, TL, 1994.

43 D. A. Pawlak, M. Ito, M. Oku, K. Shimamura and T. Fukuda, *J. Phys. Chem. B*, 2002, **106**, 504–507.

44 X. Liu, W. Dong, C. Xia, Q. Huang, Y. Cai, L. Wei, G. Wu, X. Wang, Y. Tong, Z. Qiao, Y. Meng, N. Mushtaq, B. Wang and H. Wang, *Int. J. Hydrogen Energy*, 2018, **43**, 12773–12781.

45 D. J. D. Corcoran, D. P. Tunstall and J. T. S. Irvine, *Solid State Ionics*, 2000, **136–137**, 297–303.

46 N. Wetchakun, B. Incessungvorn, K. Wetchakun and S. Phanichphant, *Mater. Lett.*, 2012, **82**, 195–198.

47 A. J. Hupfer, E. V. Monakhov, B. G. Svensson, I. Chaplygin and E. V. Lavrov, *Sci. Rep.*, 2017, **7**, 17065.

48 J. B. Bates, J. C. Wang and R. A. Perkins, *Phys. Rev. B*, 1979, **19**, 4130–4139.

49 P. Sawant, S. Varma, B. N. Wani and S. R. Bharadwaj, *Int. J. Hydrogen Energy*, 2012, **37**, 3848–3856.